



Dynamic Behavior Analysis of a Rotating Shaft with an Elliptical Breathing Surface Crack

Ahmed A. El-kashlawy¹ · Younes K. Younes¹ · Heba H. El-Mongy^{1,2} 

Received: 9 May 2022 / Revised: 17 October 2022 / Accepted: 7 December 2022 / Published online: 8 February 2023
© The Author(s) 2023

Abstract

Purpose In this paper, dynamic behavior of a rotor system with an elliptical breathing crack that simulates the real shape of the crack front is investigated.

Methods A finite element model of the cracked rotor system is developed. The crack breathing mechanism is modelled based on an improved breathing model which considers the inclination of the neutral axis of the cracked element cross-section during shaft rotation. Harmonic balance method is used to solve the equations of motion of the rotor system for steady-state response characteristics. The effect of some parameters such as crack depth, crack shape factor and the spinning speed is investigated.

Results and conclusions The results show that the unique whirl orbits behavior during passage through the subcritical speeds serve as a key indicator of crack presence in the shaft. The effects of the crack front curvature and the breathing model are revealed. The value of shape factor affects the whirl orbit characteristics such as size of the inner or outer loops and the amount by which the orbits rotate while crossing the subcritical speeds. The presented model considering the real crack front shape may contribute towards improved modelling of cracked rotors and better interpretation of measured vibration response.

Keywords Elliptical crack · Crack breathing · Cracked rotor · Finite element analysis · Harmonic balance method

Introduction

Rotating machines are widely used in engineering applications such as aircrafts, pumps, compressors, turbines, power plants, etc. In practice, most rotors operate under heavy loading conditions that may result in undesirable defects. Crack is one of these defects which is considered the most dangerous one as it may cause serious damage and loss of the machine operating lifetime. Numerous review papers summarize the various modelling and identification techniques of cracks in stationary and rotating shafts studied in previous research works [1–3]. Most recently, Kushwaha et al. [4] provided a rich survey on various modelling approaches and crack detection techniques adopted by previous researches.

Several research works provided helpful crack indicators. Al-Shudeifat et al. [5] employed the harmonic balance

approach verified by experimental work to study the effect of crack depth on the steady state dynamic behavior of a cracked rotor system. It was found that the unique behavior of the whirl orbit during passage through subcritical speeds is an indicator of presence of breathing crack in the shaft. The results showed that as the crack depth increases, resonance peaks at subcritical speeds increase. Compared with [5], Al-Shudeifat et al. [6] developed new breathing functions that accurately model the crack breathing mechanism. Then, Al-Shudeifat [7] introduced the finite element modelling of asymmetric open cracked rotor. Distinguishing features between open and breathing crack were revealed via the whirl orbits at the vicinity of the first subcritical speeds. A further improvement in the modeling of the breathing behavior of transverse cracks in rotating shafts was developed by Spagnol et al. [8]. Since the breathing crack causes asymmetry in the shaft cross section, the principle of unsymmetric bending should be utilized for accurate modeling of the breathing behavior, in which the neutral axis will be inclined with changing the rotational angles, instead of the assumed horizontal neutral axis as developed in Ref. [6]. Sinou [9] used the harmonic balance method to investigate the evolution of the super harmonic frequency components

✉ Heba H. El-Mongy
heba_almongy@m-eng.helwan.edu.eg

¹ Department of Mechanical Design, Faculty of Engineering-Matariya, Helwan University, Cairo, Egypt

² Centre for Applied Dynamics Research (CADR), School of Engineering, University of Aberdeen, Aberdeen, UK

($2X$, $3X$) in the subcritical response region as a crack presence indicator. However, it was demonstrated that these frequency components are affected by other factors such as unbalance orientation, crack depth and location. Empirical mode decomposition (EMD) was employed by Guo et al. [10] to track the change of amplitudes of the super harmonic frequency components and whirl orbits in the vicinity of $1/2$ and $1/3$ of the critical speed. Variation of these components' amplitudes can be considered as a crack indicator. However, noise may cause a limitation to the proposed method.

More crack indicators have been obtained through the investigation of the coupling phenomenon of the vibration modes due to presence of cracks [11–21]. According to this, due to crack presence, excited vibration in one direction results in vibration interaction in other directions. In Ref. [13], Darpe et al. investigated the coupling of longitudinal, torsional and lateral vibrations. Numerical work by Darpe et al. [22], and parametric experimental work by El-Mongy et al. [23] analyzed the coupling of the longitudinal and lateral steady state vibrations of a cracked Jeffcott rotor system subjected to axial excitation. Presence of axial excitation frequencies in the lateral vibration spectra represents the vibration coupling and thus a crack presence indicator. Moreover, numerical and experimental investigation of the dynamic behavior of a cracked rotor system during start-up was carried out by El-Mongy et al. [24, 25] for sub-critical analysis. It was concluded that the presence of subcritical resonances in the system's sub-critical response can be considered as a good crack detector. As the crack depth increases, more sub-critical resonances appear in the response. Darpe et al. [26] numerically and experimentally studied the breathing behavior of a cracked rotor while passing through critical speed and subharmonic resonances. Three different crack models were considered (open, switching and breathing). Higher harmonic components and orbit orientation change during passage through these subharmonic resonances provided reliable crack indicators. The effect of crack on the nonlinear response of a rotating shaft was analyzed by Sinou et al. [27] using the alternate frequency/time domain approach and path-following procedure were the crack breathing was modeled as a truncated Fourier series.

Most of the previous research on cracked rotors considered the crack front to be straight edged. However, the actual crack front usually takes an elliptical profile. Hence, the results achieved using the straight edge assumption reflect the behaviour of the idealized crack shape not the real crack behaviour. Earliest work on semi-elliptical cracks in round bars was focused on determining the stress intensity factors under bending loading [28–32] and studying fatigue crack growth under specific loading conditions as in Ref. [33]. Fonte and Freitas [34, 35] constructed an experimental rig to study fatigue crack growth of semi-elliptical cracks under bending and steady torsion loading and observed the

elliptical crack shape evolution. Rubio et al. [36] presented closed form flexibility coefficients for bending and tension taking into account the size and shape of the whole elliptical crack front. These obtained expressions were validated via calculation of static transverse displacement due to a point load. In a series of papers, Rubio et al. [37–39] presented different approaches for evaluation of the stress intensity factors of an elliptical breathing crack in a rotating shaft. Also, the dynamic behavior of rotors with elliptical cracks were investigated. Han et al. [40] studied the steady state response and dynamic instability regions of an elliptically cracked shaft. The crack was modelled using the local flexibility method. The crack front shape had significant effect on the instability regions. Di et al. [41] studied the vibration response of a rotor system with an elliptical crack. The cracked element stiffness was estimated based on the strain energy density approach that was described for the straight fronted crack in Ref. [42]. They considered the coupling of bending and torsional vibrations. The study was limited to the frequency spectra and harmonics amplitudes variation with the crack depth. Muñoz-Abella et al. [43] studied the influence of unbalance mass position on the breathing mechanism of elliptical crack on a rotating shaft. Then, in Ref. [44] they introduced an analytical expression to evaluate the first four bending natural frequencies of a nonrotating pinned–pinned Euler–Bernoulli shaft. And as an inverse problem, they proposed a genetic algorithm technique to identify elliptical crack using these known natural frequencies. Wei et al. [45] analyzed the breathing behavior of the elliptical crack and derived the cracked element stiffness matrix based on the time changing area and area moments of inertia. Spagnol et al. [46] further improved the work done in Ref. [45] to study cracks with a range of elliptical-front crack curvatures. A four-degree-of-freedom Jeffcott rotor model with massless shaft was considered by Spagnol et al. in Ref. [47]. The dynamic response was computed using Runge–Kutta numerical integration of the equations of motions in state-space form. Significant differences were found between the straight-front and elliptical front models in transverse trajectories at one-third and one-half of the critical speed.

To date, research works are still ongoing to reach closed-form expressions for flexibility coefficients of the elliptical crack (i.e. the real crack front shape). The effect of crack parameters (such as crack depth, shape factor and crack location) combined with system parameters (such as unbalance amount and orientation) needs further extensive numerical and experimental investigations. The breathing models used for the elliptical crack investigations needs further refinement to obtain more realistic results that accurately represent the dynamic behavior of elliptically cracked rotor systems.

In this paper, the dynamic behavior of a rotor system with a transverse elliptical breathing crack is studied numerically

using finite element analysis. The crack is modeled using the moment of inertia reduction approach. The present breathing model not only accounts for the real crack shape but also for the real asymmetry of the cracked cross-section where the neutral axis orientation change is taken into account rather than being assumed constantly horizontal as in Refs. [46, 47]. Harmonic balance method is used to solve the system’s equations of motion. Whirl orbits of the shaft rotating at constant speeds during crack propagation considering the effect of shape factor are studied. In addition, whirl orbits during passage through subcritical speeds are presented. Significant differences between the real elliptical front versus the assumed straight front may help in earlier crack diagnosis and in turn prevent misdiagnosis to avoid component failure.

Finite Element Modelling of Rotor System

Modeling of the Shaft

The shaft of length L is discretized into N elements with $N + 1$ nodes. Each node has four degrees of freedom consisting of two translational displacements in the X and Y directions and two rotational displacements about the X and Y directions (Fig. 1).

On assembling the equations of motion of each element, the finite element equation of motion of the whole shaft can be written as [48]:

$$\mathbf{M}\ddot{\mathbf{q}}(t) + (\mathbf{C} - \Omega\mathbf{G})\dot{\mathbf{q}}(t) + \mathbf{K}\mathbf{q}(t) = \mathbf{Q}(t) + \mathbf{F}_g, \tag{1}$$

where \mathbf{M} , \mathbf{C} , \mathbf{G} and \mathbf{K} are the shaft mass, damping, gyroscopic and stiffness matrices, respectively. Expressions of these matrices for each element can be found in Refs. [48, 49]. The vector $\mathbf{q}(t) = [\mathbf{q}_1^T \mathbf{q}_2^T \dots \mathbf{q}_i^T \dots \mathbf{q}_{N+1}^T]^T$ is the nodal displacements vector in which $\mathbf{q}_i^T(t) = [u_i \ v_i \ \varphi_i^x \ \varphi_i^y]$ is the displacement vector of a single node. Here, the excitation vector $\mathbf{Q}(t)$ is the unbalance force vector due to the unbalance mass located on the disk. The vector \mathbf{F}_g is the gravity force vector of the rotor system.

Disk Modelling

The disk is assumed to be a rigid concentrated mass in which its mass center is assumed to lie at the intersection node of

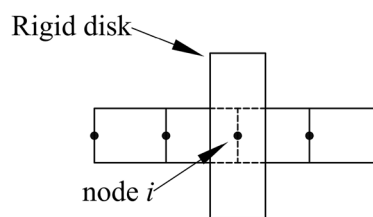


Fig. 2 Disk at node i on the shaft

two elements as shown in Fig. 2. Therefore, the disk mass center has the same displacement vector as this node.

The equation of motion of the rigid disk at node i is expressed as [5]:

$$\mathbf{M}^d\ddot{\mathbf{q}}(t) - \Omega\mathbf{G}^d\dot{\mathbf{q}}(t) = 0, \tag{2}$$

where \mathbf{M}^d , \mathbf{G}^d are the rigid disk mass and gyroscopic matrices, respectively whose expressions can be found in Refs. [5, 48].

The unbalance force vector due to the unbalance mass attached to the disk can be expressed as:

$$\mathbf{F}_u = \begin{bmatrix} me\Omega^2\cos(\Omega t + \phi) \\ me\Omega^2\sin(\Omega t + \phi) \\ 0 \\ 0 \end{bmatrix}, \tag{3}$$

where me is the unbalance amount in (kg m), Ω is the spinning speed in (rad/s) and ϕ is the initial unbalance angle with respect to the positive X axis. The system damping matrix \mathbf{C} is assumed to be proportional damping matrix and can be calculated as [50]:

$$\mathbf{C} = \alpha_d\mathbf{M} + \beta_d\mathbf{K}, \tag{4}$$

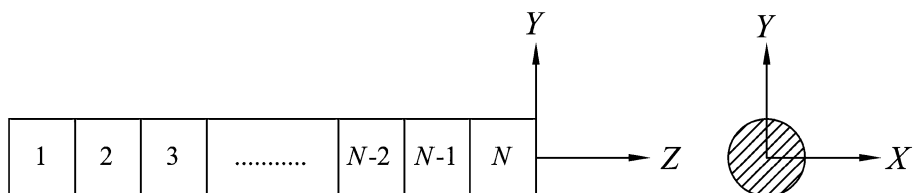
where the parameters α_d, β_d are calculated using the first two natural frequencies and first two modal damping ratios.

Crack Modelling

The crack is introduced at a cross section at the middle of the shaft. The crack front realistic shape is considered as the intersection of an ellipse with the shaft’s circular circumference [45] (Fig. 3).

Here, this ellipse has a major axis b which represents the crack depth and a minor axis a . The major centerline of that

Fig. 1 Shaft finite element model



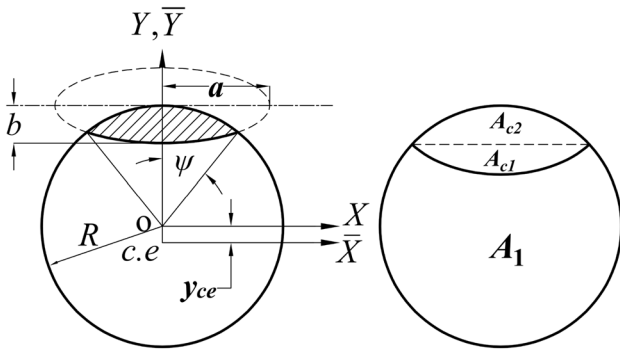


Fig. 3 Shaft cross section with a fully open elliptical crack

ellipse is always tangent to the shaft cross-section. The crack depth ratio is taken as $\mu = b/R$ and the crack front shape factor is defined as $\beta = b/a$. The shape factor gives an indication of the crack front curvature such that, as β increases, the front becomes more curved and as it decreases, the front becomes more flattened. Hence, the straight-front transverse crack is a special case of the elliptical crack where $\beta = 0$. The crack is assumed to be fully open at $t=0$ (before rotation). In this case, the area of the crack segment A_c is composed of two areas A_{c1} and A_{c2} , meanwhile, the uncracked portion of the cross section has an area A_1 . The Y -coordinate of the centroids of the areas A_{c1} , A_{c2} and A_1 are denoted respectively as $Y_c^{A_{c1}}$, $Y_c^{A_{c2}}$ and y_{ce} . The moments of inertia of the area components A_{c1} , A_{c2} about the X and Y axes are denoted as I_X^{Ac1} , I_Y^{Ac1} , I_X^{Ac2} and I_Y^{Ac2} . Then, the moments of inertia of the area A_1 about the X and Y axes are denoted as $I_X^{A_1}$ and $I_Y^{A_1}$. The moments of inertia of A_1 about the centroidal \bar{X} and \bar{Y} axes are denoted as $I_{\bar{X}}^{A_1}$ and $I_{\bar{Y}}^{A_1}$. Mathematical calculations of

these areas, centroid coordinates and moments of inertia at $t=0$ are found in Refs. [45, 46].

Crack Breathing

Due to the heavy weight of the rotor in which the static deflection dominates the deflection due to vibration, the crack was found to open and close synchronously with the shaft rotation. In other words, as the shaft rotates, the angular orientation of the neutral axis of the cross section of the cracked element keeps changing. So, at some instants, part of the crack segment becomes in the compressive stress region and so it is closed, while the other part lies in the tensile stress region and hence it remains open. This process of gradual closing and opening is called crack breathing. The angular regions where the crack closes or opens gradually and remains fully open or fully closed are described in Fig. 4.

The values of the breathing angles θ_1 and θ_2 can be calculated as:

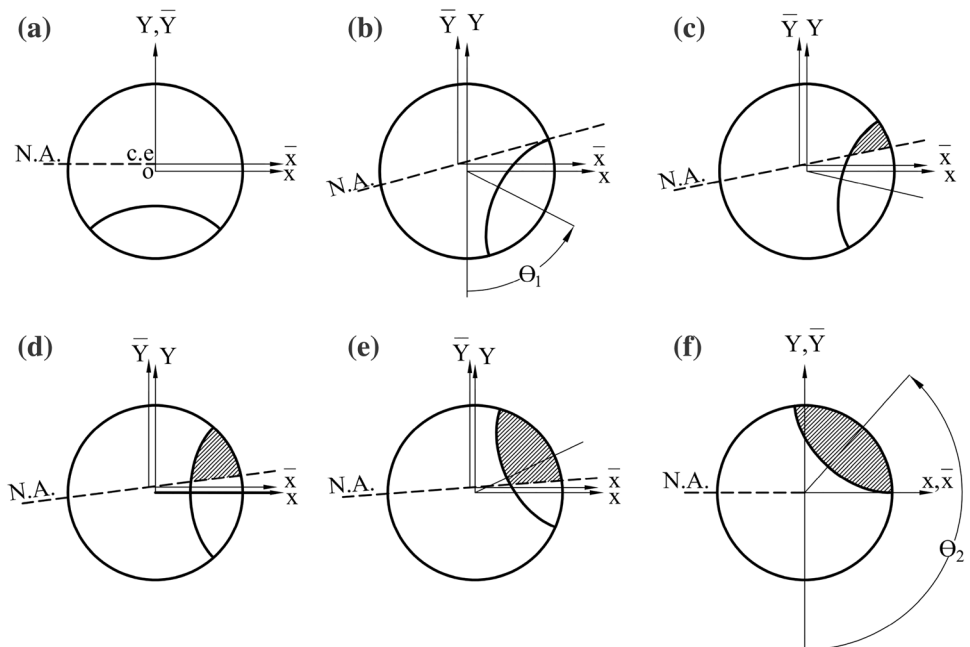
$$\theta_1 = \tan^{-1} \left(\frac{I_{\bar{Y}}^{A_1} \cdot y_{ce} + R \cos \psi}{I_{\bar{X}}^{A_1} \cdot R \sin \psi} \right), \theta_2 = \frac{\pi}{2} + \psi. \tag{5}$$

Accordingly, the time varying moments of inertia of the cracked element cross section about the fixed centroidal axes \bar{X} and \bar{Y} can now be expressed as [8, 51]:

$$\hat{I}_{\bar{X}}(t) = I - I_{11}f_1(t) \tag{6}$$

$$\hat{I}_{\bar{Y}}(t) = I + f_1(t)I_{11} + f_2(t)I_{22} \tag{7}$$

Fig. 4 Crack breathing process and the neutral axis inclination during shaft rotation



$$\widehat{I}_{XY}(t) = I_{33}f_3(t), \tag{8}$$

where $f_1(t)$, $f_2(t)$ and $f_3(t)$ are the breathing functions that model the crack breathing mechanism. Expressions of these

functions are found in Ref. [51]. The parameters, I_{11} , I_{22} and I_{33} are expressed as:

$$\begin{aligned} I_{11} &= I - (I_X^{Ac1} + I_X^{Ac2} + A_1 y_{ce}^2), \\ I_{22} &= I - (I_Y^{Ac1} + I_Y^{Ac2}), I_{33} = \frac{I_X^{A1} - I_X^{A1}}{2}. \end{aligned} \tag{9}$$

Then, the time varying cracked element stiffness matrix can be expressed as:

$$\mathbf{k}_{ce}(t) = \mathbf{k} + \mathbf{k}_1 f_1(t) + \mathbf{k}_2 f_2(t) + \mathbf{k}_3 f_3(t), \tag{10}$$

where \mathbf{k}_1 , \mathbf{k}_2 and \mathbf{k}_3 are the secondary stiffness matrices due to crack presence. Expressions of \mathbf{k}_1 , \mathbf{k}_2 can be found in Ref. [6] and expression of \mathbf{k}_3 is found in Ref. [8]. Hence, the finite element equation of motion for an unbalanced rotor system with breathing crack is written as:

$$\begin{aligned} \mathbf{M}\ddot{\mathbf{q}}(t) + (\mathbf{C} - \Omega\mathbf{G})\dot{\mathbf{q}}(t) + (\mathbf{K} + f_1(t)\mathbf{K}_1 + f_2(t)\mathbf{K}_2 \\ + f_3(t)\mathbf{K}_3)\mathbf{q}(t) = \mathbf{F}_1 \cos\Omega t + \mathbf{F}_2 \sin\Omega t + \mathbf{F}_g, \end{aligned} \tag{11}$$

where \mathbf{K}_1 , \mathbf{K}_2 , \mathbf{K}_3 are the secondary stiffness matrices of zero entries except for those corresponding to the cracked element where the entries equal to \mathbf{k}_1 , \mathbf{k}_2 , \mathbf{k}_3 respectively; \mathbf{F}_1 , \mathbf{F}_2 are the unbalance force amplitude vectors of zero entries except for those corresponding to the disk node. Expressions of \mathbf{F}_1 , \mathbf{F}_2 can be found in Ref. [5].

Steady State Solution of the System

The harmonic balance method is used to get the steady state solution of the cracked rotor system represented by Eq. (11) and shown in Fig. 5. The disk is located at the shaft midspan where the elliptical crack is located in the most adjacent element to the disk.

The solution is expressed as a finite Fourier series as:

$$\mathbf{q}(t) = \mathbf{A}_o + \sum_{k=1}^n (\mathbf{A}_k \cos(k\Omega t) + \mathbf{B}_k \sin(k\Omega t)), \tag{12}$$

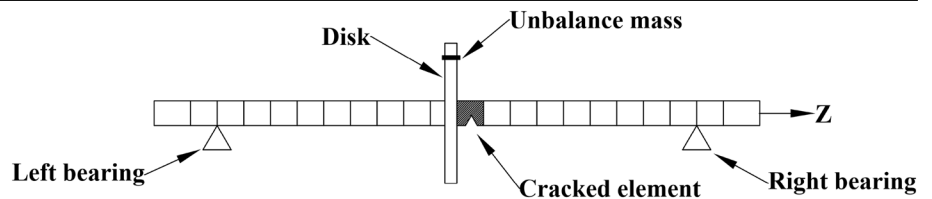
where n is the number of harmonics used. The breathing functions can be rewritten as:

$$\begin{aligned} f_1(t) &= a_o + \sum_{j=1}^m a_j \cos(j\Omega t), f_2(t) = b_o + \sum_{j=1}^{2n} b_j \cos(j\Omega t), \\ f_3(t) &= \sum_{j=1}^{2n} \gamma_j \sin(j\Omega t). \end{aligned} \tag{13}$$

Inserting this solution into Eq. (11) yields:

$$\begin{bmatrix} \tilde{\mathbf{C}} & 0.5\mathbf{C}_2^{(1)} & 0.5\mathbf{C}_{22}^{(1)} & 0.5\mathbf{C}_2^{(2)} & 0.5\mathbf{C}_{22}^{(2)} & 0.5\mathbf{C}_2^{(3)} & 0.5\mathbf{C}_{22}^{(3)} & \dots & 0.5\mathbf{C}_{22}^{(n)} \\ \mathbf{C}_2^{(1)} & \mathbf{C}_1^{(1)} & \mathbf{C}_3^{(1,1)} & \mathbf{C}_{33}^{(1,1)} & \mathbf{C}_3^{(1,2)} & \mathbf{C}_{33}^{(1,2)} & \dots & \mathbf{C}_{33}^{(1,n-1)} \\ \mathbf{C}_{22}^{(1)} & \mathbf{C}_{11}^{(1)} & \mathbf{C}_{33}^{(2,1)} & \mathbf{C}_3^{(2,1)} & \mathbf{C}_{33}^{(2,2)} & \mathbf{C}_3^{(2,2)} & \ddots & \mathbf{C}_3^{(2,n-1)} \\ \mathbf{C}_2^{(2)} & \mathbf{C}_3^{(1,1)} & \mathbf{C}_{33}^{(2,1)} & \mathbf{C}_1^{(2)} & \mathbf{C}_3^{(3,1)} & \mathbf{C}_{33}^{(3,1)} & \ddots & \mathbf{C}_{33}^{(3,n-2)} \\ \mathbf{C}_{22}^{(2)} & \mathbf{C}_{33}^{(1,1)} & \mathbf{C}_3^{(2,1)} & \mathbf{C}_{11}^{(2)} & \mathbf{C}_{33}^{(4,1)} & \mathbf{C}_3^{(4,1)} & \ddots & \mathbf{C}_3^{(4,n-2)} \\ \mathbf{C}_2^{(3)} & \mathbf{C}_3^{(1,2)} & \mathbf{C}_{33}^{(2,2)} & \mathbf{C}_3^{(3,1)} & \mathbf{C}_{33}^{(4,1)} & \mathbf{C}_1^{(3)} & \mathbf{C}_1^{(3)} & \mathbf{C}_{33}^{(5,n-3)} \\ \mathbf{C}_{22}^{(3)} & \mathbf{C}_{33}^{(1,2)} & \mathbf{C}_3^{(2,2)} & \mathbf{C}_{33}^{(3,1)} & \mathbf{C}_3^{(4,1)} & \mathbf{C}_{11}^{(3)} & \mathbf{C}_1^{(6)} & \mathbf{C}_{33}^{(5,n-3)} \\ \mathbf{C}_2^{(4)} & \mathbf{C}_3^{(1,3)} & \mathbf{C}_{33}^{(2,3)} & \mathbf{C}_3^{(3,2)} & \mathbf{C}_{33}^{(4,2)} & \mathbf{C}_3^{(5,1)} & \mathbf{C}_{33}^{(5,1)} & \mathbf{C}_3^{(2n-2,1)} \\ \vdots & \vdots & \ddots & \ddots & \ddots & \ddots & \ddots & \mathbf{C}_3^{(2n-1)} \\ \mathbf{C}_{22}^{(n)} & \mathbf{C}_{33}^{(1,n-1)} & \mathbf{C}_3^{(2,n-1)} & \mathbf{C}_{33}^{(3,n-2)} & \mathbf{C}_3^{(4,n-2)} & \mathbf{C}_{33}^{(5,n-3)} & \dots & \mathbf{C}_{11}^{(n)} & \mathbf{C}_{2n}^{(n)} \end{bmatrix} \begin{bmatrix} \mathbf{A}_o \\ \mathbf{A}_1 \\ \mathbf{B}_1 \\ \mathbf{A}_2 \\ \mathbf{B}_2 \\ \vdots \\ \mathbf{A}_{n-1} \\ \mathbf{B}_{n-1} \\ \mathbf{A}_n \\ \mathbf{B}_n \end{bmatrix} = \begin{bmatrix} \mathbf{F}_g \\ \mathbf{F}_1 \\ \mathbf{F}_2 \\ 0 \\ 0 \\ 0 \\ 0 \\ 0 \\ 0 \end{bmatrix}, \tag{14}$$

Fig. 5 Finite element model of the rotor system assembly



where $\tilde{\mathbf{C}} = \mathbf{K} + a_o \mathbf{K}_1 + b_o \mathbf{K}_2$ and $\mathbf{C}^{(i)} = \tilde{\mathbf{C}} - ((i + 1)\Omega/2)^2 \mathbf{M} + \frac{1}{2}(a_{i+1} \mathbf{K}_1 + b_{i+1} \mathbf{K}_2)$ for odd values of i ($i = 1, 3, 5, \dots, 2n - 1$) and $\mathbf{C}^{(i)} = \tilde{\mathbf{C}} - (i\Omega/2)^2 \mathbf{M} - \frac{1}{2}(a_i \mathbf{K}_1 + b_i \mathbf{K}_2)$ for even values of i ($i = 2, 4, 6, \dots, 2n$) and $\mathbf{C}_{11}^{(i)} = i\Omega(\mathbf{C} - \Omega \mathbf{G}) + \frac{1}{2}\gamma_i \mathbf{K}_3$ for ($i = 1, 2, \dots, n$) and $\mathbf{C}_{11}^{(i)} = -i\Omega(\mathbf{C} - \Omega \mathbf{G}) + \frac{1}{2}\gamma_i \mathbf{K}_3$ and $\mathbf{C}_{22}^{(i)} = \gamma_i \mathbf{K}_3$ and $\mathbf{C}_3^{(k,i)} = \frac{1}{2}[(a_{i+k+1} + a_i) \mathbf{K}_1 + (b_{i+k+1} + b_i) \mathbf{K}_2]$ for odd values of k ($k = 1, 3, 5, \dots, 2n - 3$) and $\mathbf{C}_3^{(k,i)} = \frac{1}{2}[(a_i - a_{i+k}) \mathbf{K}_1 + (b_i - b_{i+k}) \mathbf{K}_2]$ for even values of k ($k = 2, 4, 6, \dots, 2n - 2$) and $\mathbf{C}_{33}^{(k,i)} = \frac{1}{2}(\gamma_{i+k+1} + \gamma_i) \mathbf{K}_3$ for odd values of k ($k = 1, 3, 5, \dots, 2n - 3$) and $\mathbf{C}_{33}^{(k,i)} = \frac{1}{2}(\gamma_i - \gamma_{i+k}) \mathbf{K}_3$ for even values of k ($k = 2, 4, 6, \dots, 2n - 2$).

Note that, in this case the \mathbf{Z} matrix is of size $((2n + 1) \times S, (2n + 1) \times S)$

Results and Discussion

Geometrical and material data of the rotor system are given in Table 1. A MATLAB® code is used to build the finite element model of the system and perform the numerical calculations. The shaft is divided into 22 Euler–Bernoulli beam elements. Steady state response is evaluated using the harmonic balance method with 8 harmonics.

The horizontal and vertical vibration responses (denoted as u and v , respectively) are calculated at the node where the disk is located. The whirl amplitude is then calculated as $\sqrt{u^2 + v^2}$. From the eigen value analysis of the uncracked simply supported system, the first bending natural frequency Ω_{cr1} is obtained as ≈ 124 Hz.

Table 1 Parameters of the rotor system

Parameter	Value
Shaft	
Length	500 mm
Outer diameter	20 mm
Bearing span	410 mm
Material density	7800 kg/m ³
Modulus of elasticity	2×10^{11} N/m ²
Poisson ratio	0.3
Disk	
Thickness	11.22 mm
Outer diameter	150 mm
Inner diameter	20 mm
Mass	1.52 kg
Mass unbalance ($m.e$)	2.5×10^{-4} kg m unless otherwise stated
Unbalance angle (ϕ)	0°

To validate the model, the Newmark integration method (with parameters $\alpha_N = 0.25$ and $\delta_N = 0.5$ [50]) was used to obtain the response and compare with the results obtained from the Harmonic balance method (HBM). Arbitrary different cases of crack depth, shape factor and spinning speed were chosen for the validation process. The spinning speeds were chosen around the subcritical speed zones.

For a low crack depth ($\mu = 0.2$), validation was made for both straight crack front (i.e. $\beta = 0$) as shown in Fig. 6; and elliptical front with $\beta = 0.5$ as shown in Fig. 7. Speeds were chosen during passage through 1/4th, 1/3rd and 1/2 of the respective first critical speed of the rotor. Similarly, Figs. 8 and 9 present the validation results for crack depth $\mu = 0.3$ (with $\beta = 0$ and $\beta = 1$) but with the same set of rotating speeds (during passage through 1/4th and 1/5th of the first critical speed). Validation for moderately high crack depths is also presented in Fig. 10 for $\mu = 0.4$ and $\beta = 1/3$; and Fig. 11 for $\mu = 0.5$ and $\beta = 0.5$, at arbitrarily chosen rotational speeds. As shown in the figures, the two solution methods showed very good agreement with different values of system and crack parameters.

Effect of the Shape Factor on the Subcritical Resonances

Results of the whirl amplitudes versus the rotational speed revealed the subcritical resonance speeds in the form of emerging peaks which are considered an indicator of breathing crack presence as shown in Fig. 12. Each case is drawn by varying the value of the shape factor at constant crack depth to show the crack front curvature effect on the system critical speeds. Here, this effect can be noticed as the existing shift in critical speeds compared with the straight front assumption (i.e. $\beta = 0$). It can be noticed also that as the shape factor increases, shifting in peaks increases. Also, as the crack depth increases, more sub-resonance peaks appear as shown in Fig. 12c. It can be seen that relying on the crack indicator related to the subcritical speeds corresponding to the straight front can lead to crack misdiagnosis which in turn may expose the system to failure especially at deeper cracks.

Whirl Orbits at Different Crack Depths and Shape Factors at Constant Rotational Speeds

The constant rotational speeds are chosen here as integer submultiples of the first critical speed of an intermediate case of crack depth and shape factor from the cases shown in Fig. 12. The effect of the crack shape factor and crack depth is shown in Figs. 13 and 14 at speeds (1847.4 rpm) and (3694 rpm) respectively.

Variation of the whirling response can be witnessed in the orbit plots in Fig. 13 as the crack propagates at different

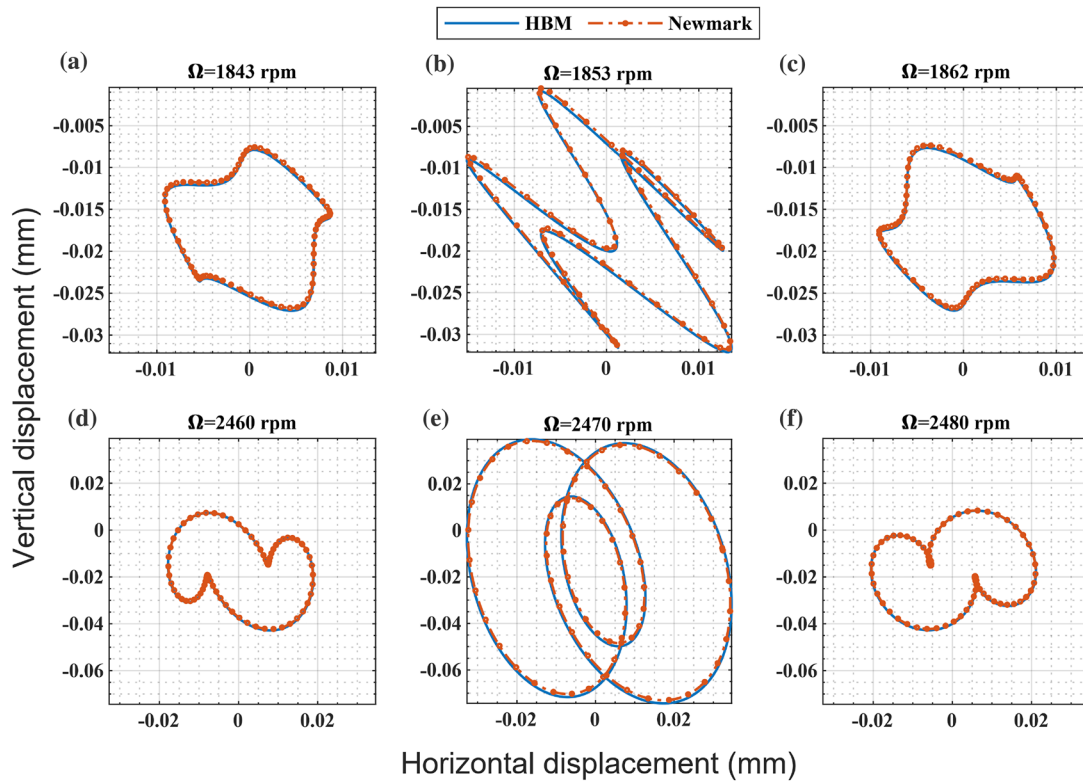


Fig. 6 Comparison of whirl orbits for straight crack front for $\mu=0.2$ using harmonic balance method and Newmark method during passing the fourth and third of the first critical speed

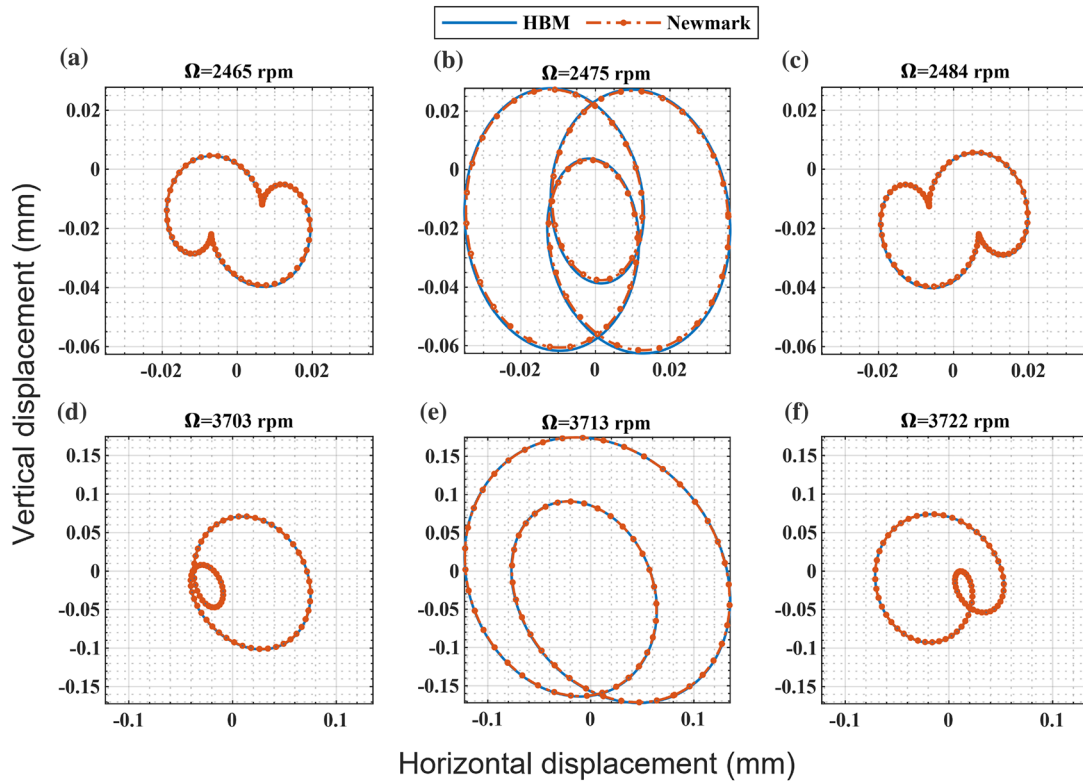


Fig. 7 Comparison of whirl orbits for elliptical crack front for $\mu=0.2$ and $\beta=0.5$ using harmonic balance method and Newmark method during passing the third and half of the first critical speed

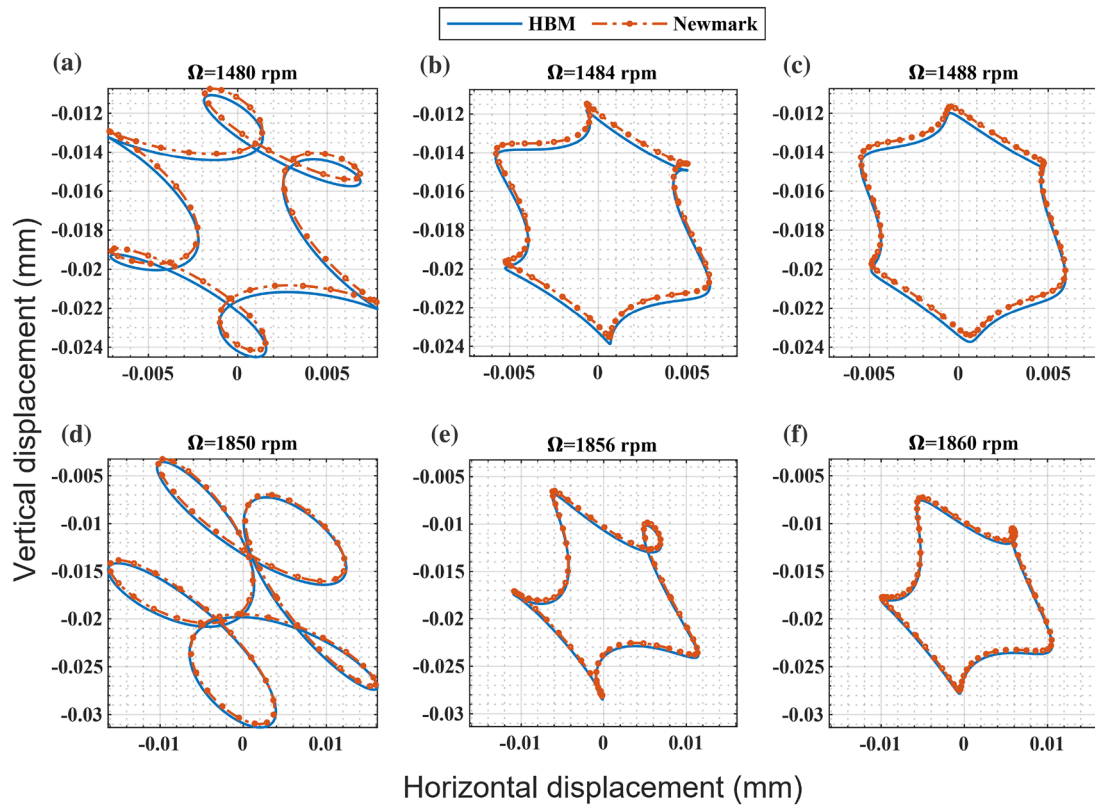


Fig. 8 Comparison of whirl orbits for straight crack front for $\mu=0.3$ using harmonic balance method and Newmark method during passing the fourth and fifth of the first critical speed

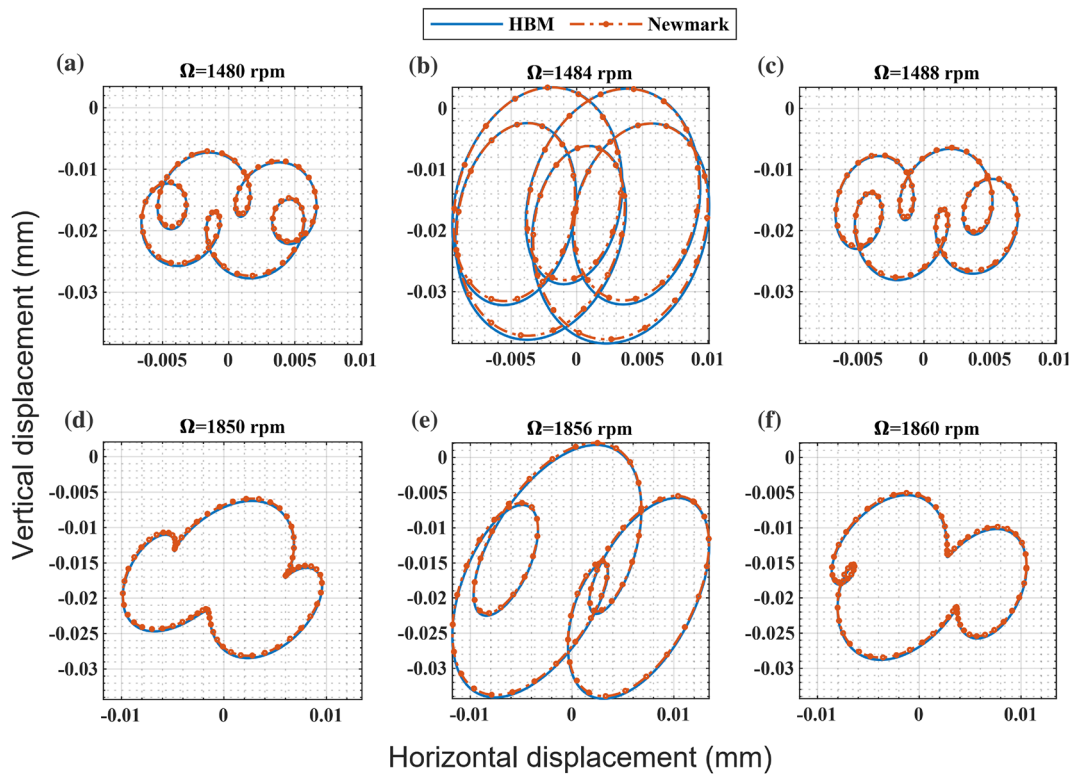


Fig. 9 Comparison of whirl orbits for elliptical crack front for $\mu=0.3$ and $\beta=1$ using harmonic balance method and Newmark method during passing the fourth and fifth of the first critical speed

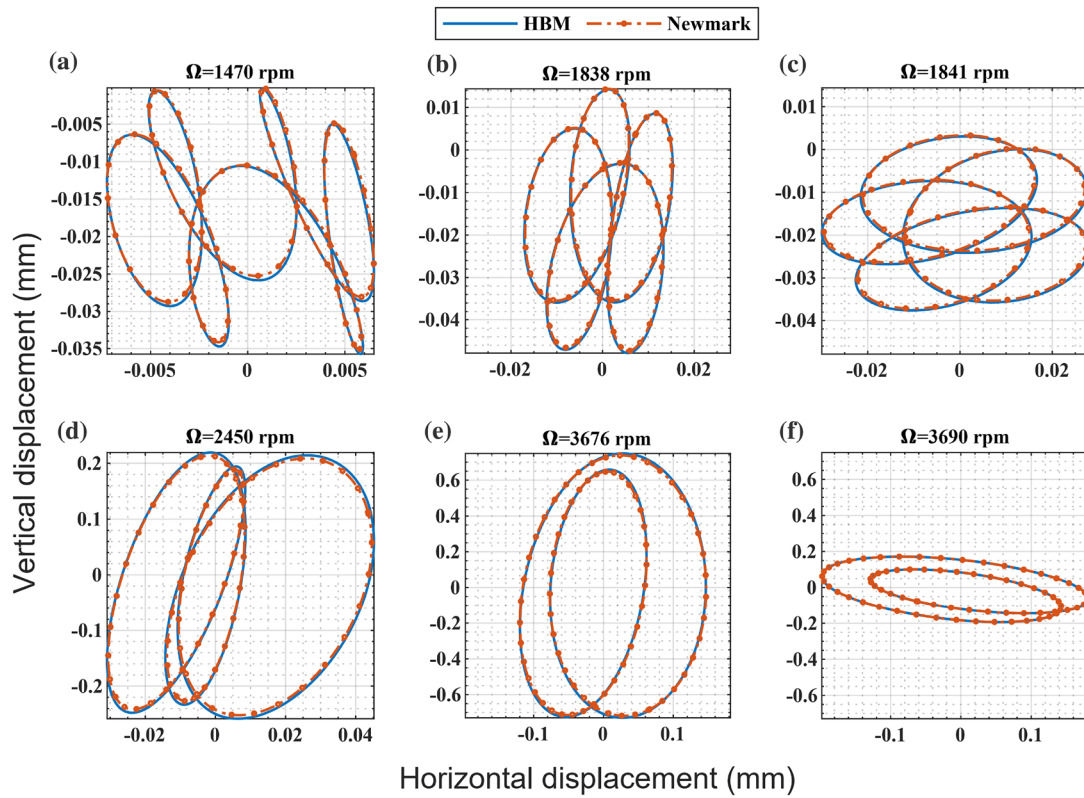


Fig. 10 Comparison of whirl orbits for elliptical crack front for $\mu=0.4$ and $\beta=1/3$ using harmonic balance method and Newmark method at different speeds

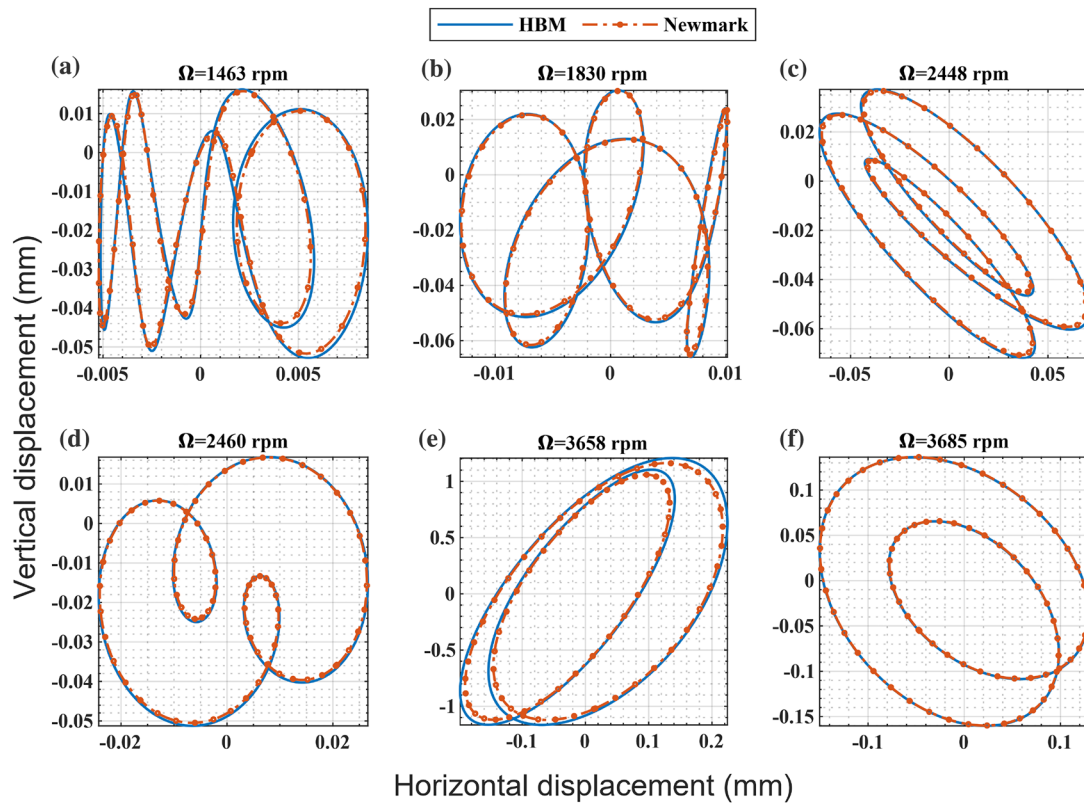


Fig. 11 Comparison of whirl orbits for elliptical crack front for $\mu=0.5$ and $\beta=0.5$ using harmonic balance method and Newmark method at different speeds

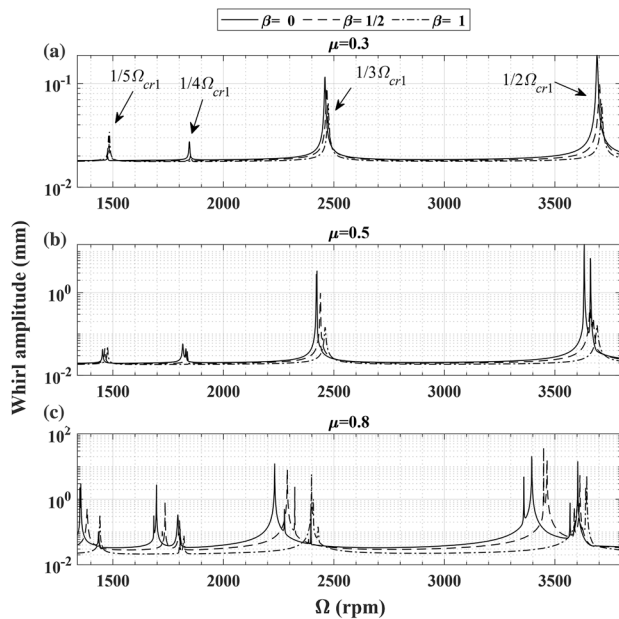


Fig. 12 Peaks of subcritical speeds at different values of crack depths and shape factors: **a** $\mu=0.3$, **b** $\mu=0.5$, **c** $\mu=0.8$. at $m.e = 1 \times 10^{-6}$ kg m

shape factors. It is observed that at this speed with small crack depth ($\mu=0.2$), no loops are formed in the whirl orbits. At $\mu=0.3$ and $\mu=0.5$, it can be noticed that both orientation and shape of the orbits are varied with changing the shape factor β which indicates corresponding change in the amplitude and phase of the vibration response. The loops appearing in the orbits clearly indicate the presence of higher harmonics in the crack response which is a well-known crack signature [10, 26, 52]. At higher crack depth, $\mu=0.8$, it can be observed that the change in the orbit becomes less pronounced.

Figure 14 shows the evolution of whirl orbits at half the first critical speed for different crack depths and shape factors. The inner loop indicating the presence of second harmonic component is observed clearly which is a known crack indicator at this speed. However, the shape factor has an obvious effect on the shape of the orbits. For $\mu=0.2$, the inner loop is getting smaller with the increase of the shape factor and it disappears for $\beta=1$. It is also noticed that at a constant shape factor, the orbit experiences a change in its orientation by about π rad as the crack propagates (see Fig. 14f, i) which agrees well with previous literature as [26]. All these changes demonstrate the variations that occur in the amplitude and phase of the vibration response of the cracked rotor when the crack shape is taken into consideration.

Whirl Orbits During Passage Through Subcritical Resonances

The whirl orbits of the system while passing through the subcritical speeds are plotted in Figs. 15 and 16 at crack depth $\mu=0.3$ for two shape factors $\beta=0.5$ and $\beta=1$ respectively. The orbit plots corresponding to the straight crack front ($\beta=0$) are plotted on the same axes of other shape factor values for comparison. The stiffness variation due to breathing of the elliptical crack in the rotating coordinate system gives rise to higher harmonics in the nonlinear system response as can be seen in the orbit shapes in both Figs. 15 and 16. This stiffness variation affects the frequency content of the response during passage through the sub-critical speeds [9, 26]. For example, the forward whirl orbits at $\mu=0.3$, $\beta=0.5$ while crossing 1/5th of the first critical speed Ω_{cr1} (in this case $1/5 \Omega_{cr1} \approx 1480.6$ rpm) shown in Fig. 15a–c, the 5X harmonic component dominates the system response. This is also indicated by formation of the four inner loops in the orbits. It can be noticed that the size of the inner loops gets larger as the speed approaches the subcritical speed, and then gets smaller as the speed increases away from the subcritical speed. Orbit orientation change can be observed while crossing the subcritical speed. Meanwhile, significant different orbit shape, size and direction is noticed in case of the assumed straight crack front. Here the orbit has five outer loops whose size decays earlier as the speed increases.

Similar observations can be seen in case of 1/3rd the first critical speed as in Fig. 15d–f. Here, the response is dominated by the 3X frequency component. The orbit has two inner loops and rotates by about $\pi/2$ rad as it crosses the subcritical speed. In this case, the difference between the elliptical and straight crack is less noticeable compared with the previous case. In Fig. 15g–i, orbits during passage through 1/2 the first critical speed where the response is dominated by the 2X component. The forward whirl orbit is characterized by the inner loop and rotates by about $\pi/2$ rad as it crosses the subcritical speed. In this case, difference between the models is less noticeable compared with the previous two cases except that the orbit rotates by a smaller amount ($\approx \pi/4$ rad). It can be noticed that the orbit size of the elliptical crack is smaller than that of the straight crack before the subcritical speed zone as shown in Fig. 15a, d, g; and larger at the subcritical speed zone (Fig. 15b, e, h); then slightly larger after the subcritical speed zone (Fig. 15c, f, i).

Figure 16 shows the whirl orbits during passage through the 1/5th and 1/4th of the first critical speed at $\mu=0.3$ for the case $\beta=1$ (i.e. circular front). The orbits in Fig. 16a–c show similar observations as those in Fig. 15a–c in case of $\beta=0.5$ except for the relative orientation of the orbit loops among the two cases. Figure 16d–f presents forward whirl orbits

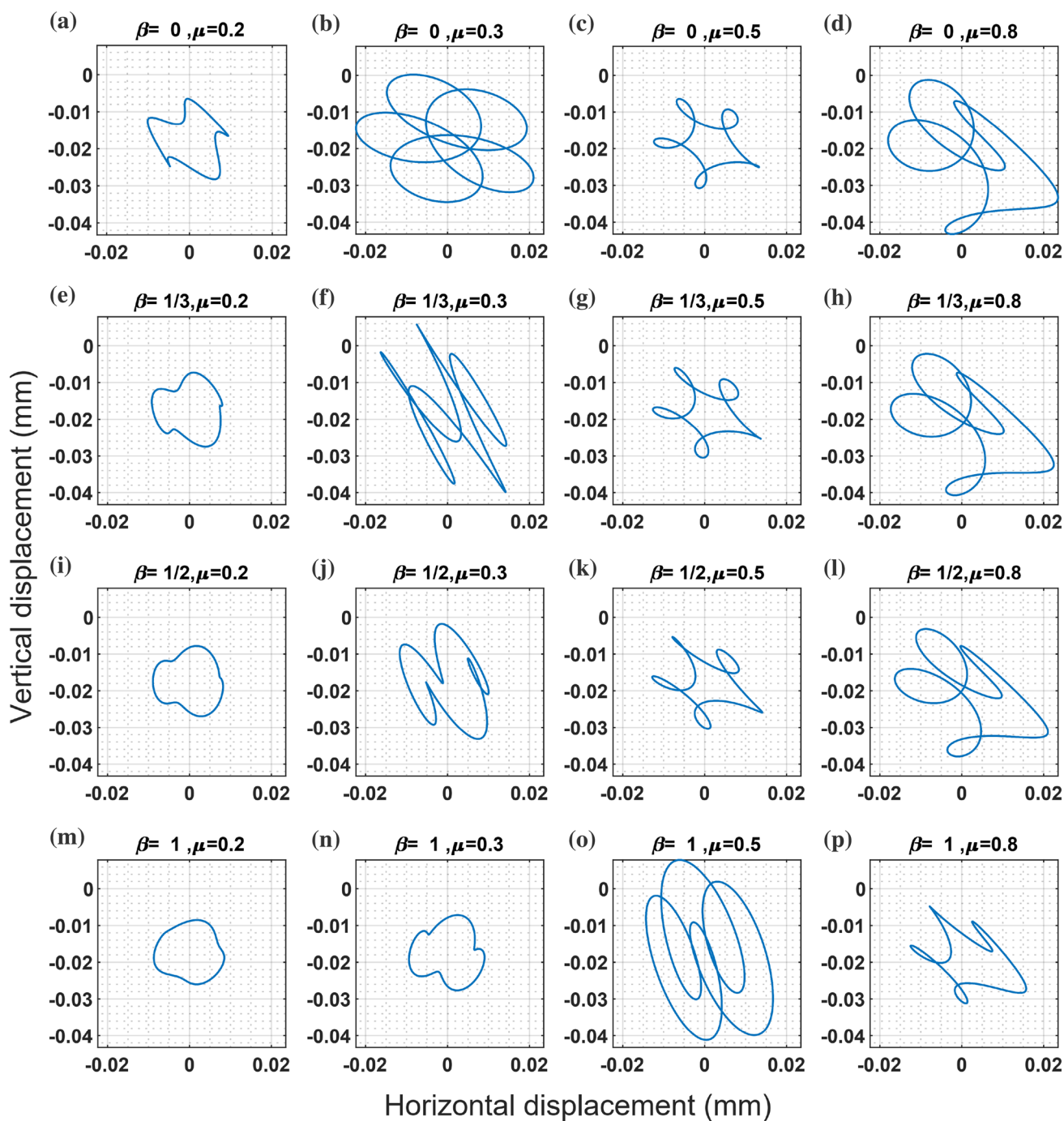


Fig. 13 Evolution of the system whirl orbits at different values of crack depths and shape factors at $\Omega = 1847.4$ rpm, $m.e = 2.5 \times 10^{-4}$ kg m

while passage through 1/4th of the first critical speed. Here the 4X component is dominant but on a narrow range of rotational speeds as evident by the three inner loops. In addition, the relative orientation of the orbit inner loops gets distorted to some extent while crossing the subcritical speed. Meanwhile, for the straight front model, different whirl direction is observed. In this case, the orbit is backward with five outer loops with decreasing size with the speed.

Conclusions

In this paper, the finite element model of a rotor system with a transverse elliptical breathing crack is developed to investigate the system’s steady state response using the harmonic balance method. Crack breathing mechanism is modeled through the time varying area moments of inertia approach taking into account the neutral axis inclination

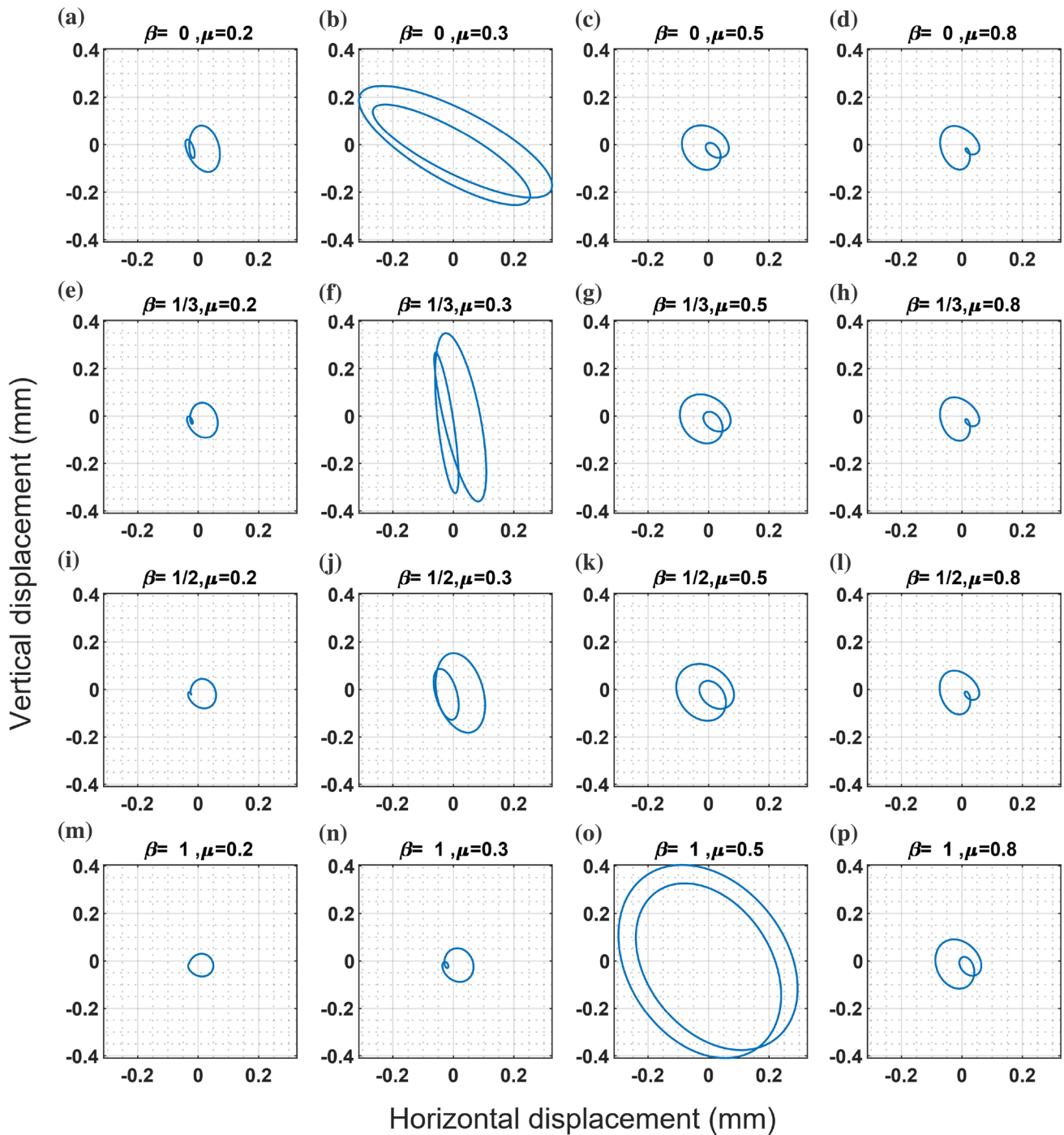


Fig. 14 Evolution of the system whirl orbits at different values of crack depths and shape factors at $\Omega = 3694$ rpm, $m.e = 2.5 \times 10^{-4}$ kg m

change. The major findings of this work are summarized as follows. Presence of the breathing elliptical crack can be tracked using the super harmonic frequency components in the system subcritical response. Whirl orbits in the vicinity of the subcritical speeds introduced unique shapes and

orientation and in turn serve as a key detector of crack presence. Compared to the assumed straight crack front, shape factors can affect the whirl orbit characteristics such as the size of the inner or outer loops and the amount

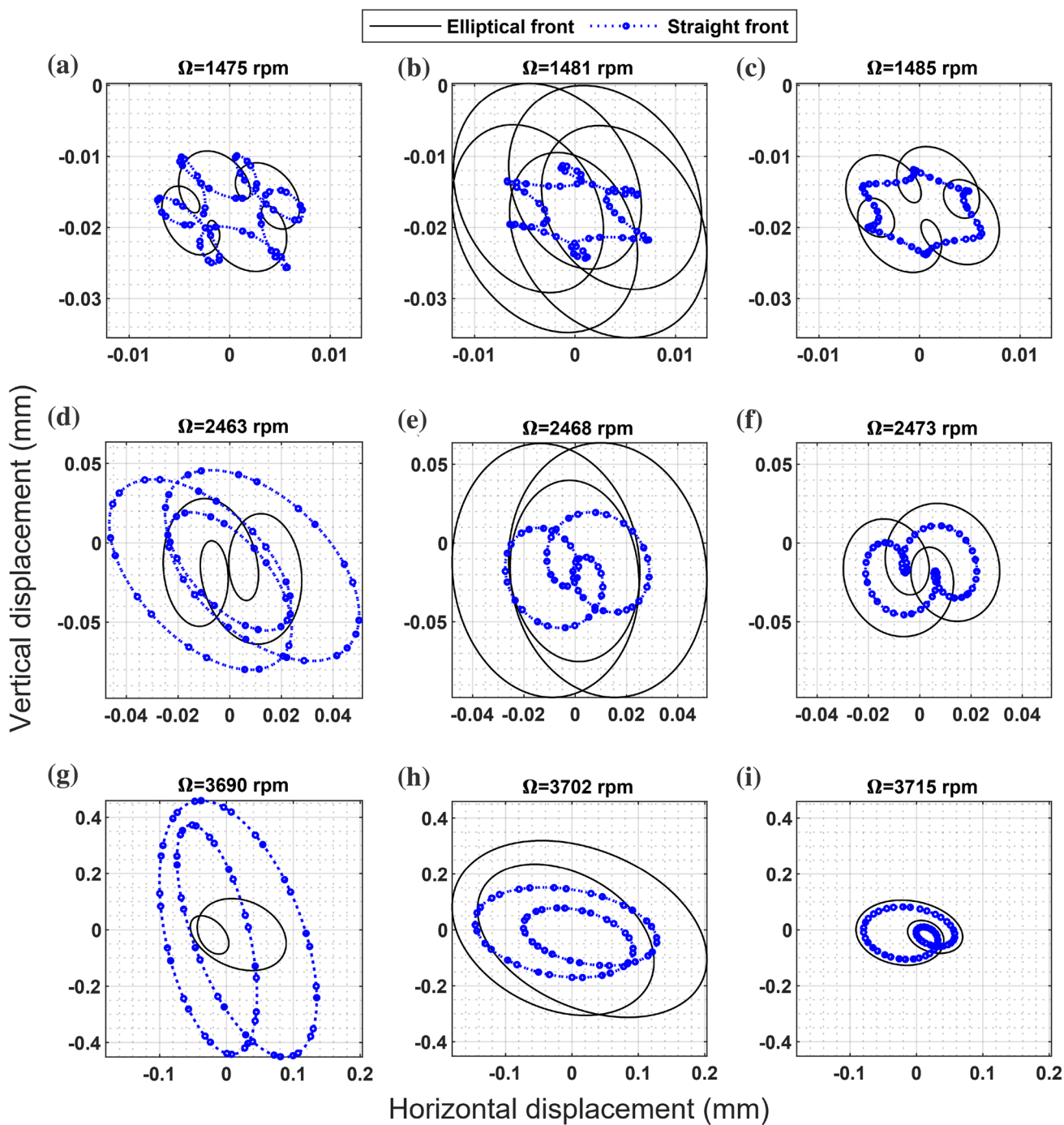


Fig. 15 Whirl orbits at $\mu=0.3$, $\beta=0.5$ during passage through the subcritical speeds, **a–c** through $1/5 \Omega_{cr1} \approx 1480.6$ rpm, **d–f** through $1/3 \Omega_{cr1} \approx 2468$ rpm, **g–i** through $1/2 \Omega_{cr1} \approx 3702$ rpm. for $m.e = 2.5 \times 10^{-4}$ kg m

by which the orbits rotate while crossing the subcritical speeds. The present breathing model that considers the effects of the elliptical crack shape, the non-symmetric cracked cross section and the neutral axis inclination angle

provides closer simulation of real cracked rotors. Hence, consideration of these effects may help in earlier crack diagnosis and better modelling of crack effects on the vibration response.

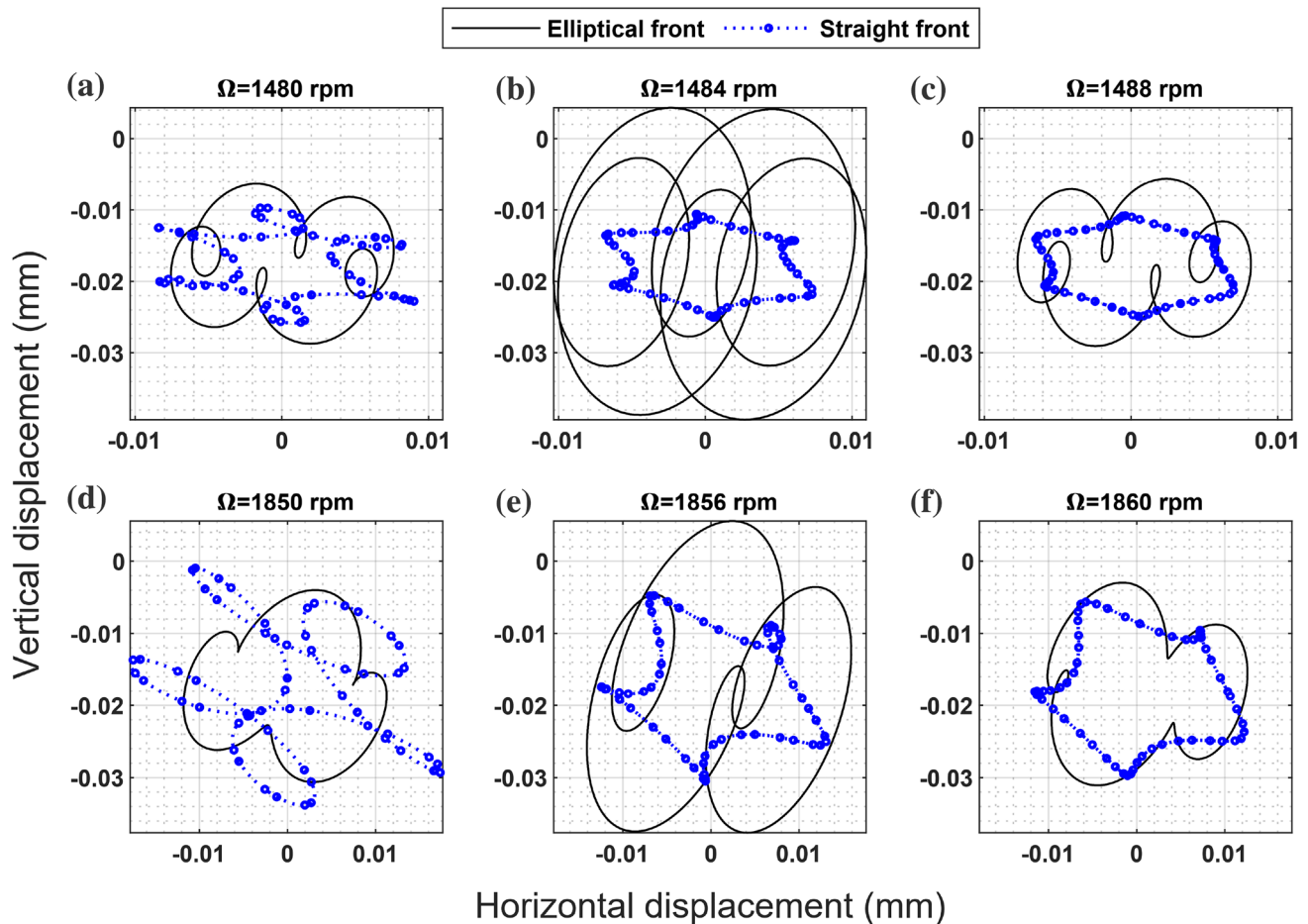


Fig. 16 Whirl orbits at $\mu=0.3$, $\beta=1$ during passage through the subcritical speeds, **a–c** through $1/5\Omega_{cr1} \approx 1484$ rpm, **d–f** through $1/4\Omega_{cr1} \approx 1856$ rpm for $m.e = 2.5 \times 10^{-4}$ kg m

Acknowledgements The authors would like to thank the anonymous reviewers for their valuable suggestions that helped in improving the manuscript.

Data availability Data will be made available on reasonable request.

Declarations

Conflict of interest On behalf of all authors, the corresponding author states that there is no conflict of interest.

Open Access This article is licensed under a Creative Commons Attribution 4.0 International License, which permits use, sharing, adaptation, distribution and reproduction in any medium or format, as long as you give appropriate credit to the original author(s) and the source, provide a link to the Creative Commons licence, and indicate if changes were made. The images or other third party material in this article are included in the article's Creative Commons licence, unless indicated otherwise in a credit line to the material. If material is not included in the article's Creative Commons licence and your intended use is not permitted by statutory regulation or exceeds the permitted use, you will need to obtain permission directly from the copyright holder. To view a copy of this licence, visit <http://creativecommons.org/licenses/by/4.0/>.

References

1. Dimarogonas AD (1996) Vibration of cracked structures: a state of the art review. *Eng Fract Mech* 55(5):831–857
2. Gasch R (1993) A survey of the dynamic behaviour of a simple rotating shaft with a transverse crack. *J Sound Vib* 160(2):313–332
3. Sabnavis G et al (2004) Cracked shaft detection and diagnostics: a literature review. *Shock Vib Digest* 36(4):287
4. Kushwaha N, Patel V (2020) Modelling and analysis of a cracked rotor: a review of the literature and its implications. *Arch Appl Mech* 90(6):1215–1245
5. Al-Shudeifat MA, Butcher EA, Stern CR (2010) General harmonic balance solution of a cracked rotor-bearing-disk system for harmonic and sub-harmonic analysis: analytical and experimental approach. *Int J Eng Sci* 48(10):921–935
6. Al-Shudeifat MA, Butcher EA (2011) New breathing functions for the transverse breathing crack of the cracked rotor system: approach for critical and subcritical harmonic analysis. *J Sound Vib* 330(3):526–544
7. AL-Shudeifat MA (2013) On the finite element modeling of the asymmetric cracked rotor. *J Sound Vib* 332(11):2795–2807
8. Spagnol J, Wu H, Yang C (2020) Application of non-symmetric bending principles on modelling fatigue crack behaviour and vibration of a cracked rotor. *Appl Sci* 10(2):717

9. Sinou J-J (2008) Detection of cracks in rotor based on the 2 \times and 3 \times super-harmonic frequency components and the crack-unbalance interactions. *Commun Nonlinear Sci Numer Simul* 13(9):2024–2040
10. Guo C et al (2013) Application of empirical mode decomposition to a Jeffcott rotor with a breathing crack. *J Sound Vib* 332(16):3881–3892
11. Chasalevris A, Papadopoulos C (2006) Cross coupled bending vibrations of rotating shaft due to a transverse breathing crack. In: Seventh IFToMM conference on rotor dynamics, Vienna, Austria
12. Chasalevris A, Papadopoulos CA (2008) Coupled horizontal and vertical bending vibrations of a stationary shaft with two cracks. *J Sound Vib* 309(3–5):507–528
13. Darpe A, Gupta K, Chawla A (2004) Coupled bending, longitudinal and torsional vibrations of a cracked rotor. *J Sound Vib* 269(1):33–60
14. Giannopoulos G et al (2015) Coupled vibration response of a shaft with a breathing crack. *J Sound Vib* 336:191–206
15. Gounaris G et al (1996) Crack identification in beams by coupled response measurements. *Comput Struct* 58(2):299–305
16. Ostachowicz W, Krawczuk M (1992) Coupled torsional and bending vibrations of a rotor with an open crack. *Arch Appl Mech* 62(3):191–201
17. Papadopoulos C, Dimarogonas A (1988) Stability of cracked rotors in the coupled vibration mode. *J Vib Acoust Stress Reliab Des* 110(3):356–359
18. Papadopoulos C, Dimarogonas A (1988) Coupled longitudinal and bending vibrations of a cracked shaft. *J Vib Acoust Stress Reliab Des* 110(1):1–8
19. Papadopoulos C, Dimarogonas A (1992) Coupled vibration of cracked shafts. *J Vib Acoust* 114(4):461–467
20. Papadopoulos C, Dimarogonas A (1987) Coupled longitudinal and bending vibrations of a rotating shaft with an open crack. *J Sound Vib* 117(1):81–93
21. Zhang B, Li Y (2014) Six degrees of freedom coupled dynamic response of rotor with a transverse breathing crack. *Nonlinear Dyn* 78(3):1843–1861
22. Darpe A et al (2002) Analysis of the response of a cracked Jeffcott rotor to axial excitation. *J Sound Vib* 249(3):429–445
23. El-Mongy HH, Younes YK, El-Morsy MS (2015) Vibrational characteristics of a cracked rotor subjected to periodic auxiliary axial excitation. In: *Vibration engineering and technology of machinery*, Springer, pp 777–787
24. El-Mongy HH, Younes YK (2018) Vibration analysis of a multi-fault transient rotor passing through sub-critical resonances. *J Vib Control* 24(14):2986–3009
25. El-Mongy HH, Younes YK (2015) Vibrational behaviour of a transient cracked rotor: sub-critical and past-critical analyses. *Eng Res J* 146:M69–M92
26. Darpe A, Gupta K, Chawla A (2004) Transient response and breathing behaviour of a cracked Jeffcott rotor. *J Sound Vib* 272(1):207–243
27. Sinou J-J, Lees A (2005) The influence of cracks in rotating shafts. *J Sound Vib* 285(4–5):1015–1037
28. Shiratori M et al (1987) Analysis and application of influence coefficients for round bar with a semi-elliptical surface crack. *Handb Stress Intensity Factors* 2:659–665
29. Murakami Y (1987) Stress-intensity factor equations for a semi-elliptical surface crack in a shaft under bending. *Stress Intensity Factors Handb* 2:657–667
30. de Fonte M, Gomes E, de Freitas M (1999) Stress intensity factors for semi-elliptical surface cracks in round bars subjected to mode I (bending) and mode III (torsion) loading. In: *European Structural Integrity Society*. Elsevier, pp 249–260
31. Da Fonte M, De Freitas M (1999) Stress intensity factors for semi-elliptical surface cracks in round bars under bending and torsion. *Int J Fatigue* 21(5):457–463
32. Fonte M, Freitas M. Stress intensity factors for two critical angular positions of semi-elliptical surface cracks in shafts. In: Selvadurai APS, Brebbia CA, editors. *Damage and fracture mechanics VI – computer aided assessment and control*. pp 491–500
33. Carpinteri A (1992) Elliptical-arc surface cracks in round bars. *Fatigue Fract Eng Mater Struct* 15(11):1141–1153
34. Fonte M, Freitas M (1994) Fatigue crack growth under rotating bending and steady torsion. In: *Proceedings of the fourth international conference on biaxial/multiaxial fatigue* 94, vol 1, pp 159–170
35. Fonte MA, de Freitas MM (1970) Fatigue crack growth of semi-elliptical cracks under bending combined with steady torsion. *WIT Trans Eng Sci* 13:927–934
36. Rubio L, Muñoz-Abella B, Loaliza G (2011) Static behaviour of a shaft with an elliptical crack. *Mech Syst Signal Process* 25(5):1674–1686
37. Rubio P, Muñoz-Abella B, Rubio L (2015) FEM analysis of the SIF in rotating shafts containing breathing elliptical cracks. In: *Proceedings of the 9th IFToMM international conference on rotor dynamics*. Springer
38. Rubio P et al (2015) Determination of the stress intensity factor of an elliptical breathing crack in a rotating shaft. *Int J Fatigue* 77:216–231
39. Rubio P, Muñoz-Abella B, Rubio L (2018) Neural approach to estimate the stress intensity factor of semi-elliptical cracks in rotating cracked shafts in bending. *Fatigue Fract Eng Mater Struct* 41(3):539–550
40. Han Q, Chu F (2012) Dynamic instability and steady-state response of an elliptical cracked shaft. *Arch Appl Mech* 82(5):709–722
41. Di Y, Liu CL, Zhang QD, Cheng W, Zhou, SP (2012) Dynamic analysis of the rotor system with a semi-elliptical fronted crack on the shaft. In: *Applied Mechanics and Materials*, Trans Tech Publications Ltd., Vol. 226, pp. 665–671
42. Dimarogonas AD, Paipetis SA, Chondros TG (2013) *Analytical methods in rotor dynamics*. Springer Science & Business Media, Berlin
43. Muñoz-Abella B et al (2012) Study of the breathing mechanism of an elliptical crack in a rotating shaft with an eccentric mass. In: *Proceedings of the World congress on computational mechanics*, Sao Paulo, Brazil
44. Muñoz-Abella B et al (2018) Elliptical crack identification in a nonrotating shaft. *Shock Vib* 2018:4623035
45. Wei X et al (2014) Time-varying stiffness analysis on rotating shaft with elliptical-front crack. *Int J Ind Syst Eng* 17(3):302–314
46. Spagnol JP, Wu H (2016) The effect of elliptical-front crack shape on the breathing mechanism of a crack in a rotating shaft. In: *Proceedings of acoustics 2016: the second Australasian acoustical societies conference*, 9–11 November 2016, Brisbane, Queensland, Australia
47. Spagnol J, Wu H, Yang C (2019) Effects of elliptical crack shape ratio on transverse trajectory of a cracked. In: *Robotics and mechatronics: Proceedings of the fifth IFToMM international symposium on robotics and mechatronics (ISRMM 2017)*. Springer
48. Tiwari R (2017) *Rotor systems: analysis and identification*. CRC Press, Boca Raton
49. Lalanne M, Ferraris G (1998) *Rotordynamics prediction in engineering*. Wiley, New York
50. Bathe K-J (2006) *Finite element procedures*. Klaus-Jurgen Bathe, Berlin
51. Guo C et al (2013) Stability analysis for transverse breathing cracks in rotor systems. *Eur J Mech A Solids* 42:27–34
52. Sinou JJ, Lees AW (2007) A non-linear study of a cracked rotor. *Eur J Mech A Solids* 26(1):152–170